

3. Laser Raman Spectroscopy

For many years Raman spectroscopy has been a powerful tool for the investigation of molecular vibrations and rotations. In the pre-laser era, however, its main drawback was a lack of sufficiently intense radiation sources. The introduction of lasers, therefore, has indeed revolutionized this classical field of spectroscopy. Lasers have not only greatly enhanced the sensitivity of spontaneous Raman spectroscopy but they have furthermore initiated new spectroscopic techniques, based on the stimulated Raman effect, such as coherent anti-Stokes Raman scattering (CARS) or hyper-Raman spectroscopy. The research activities in laser Raman spectroscopy have recently shown an impressive expansion and a vast literature on this field is available. In this chapter we summarize only briefly the basic background of the Raman effect and present some experimental techniques that have been developed for Raman spectroscopy of gaseous media. For more thorough studies of this interesting field the textbooks and reviews given in [3.1–3.12] and the conference proceedings [3.13, 3.14] are recommended. More information on Raman spectroscopy of liquids and solids can be found in [3.11, 3.15–3.18].

3.1 Basic Considerations

Raman scattering may be regarded as an inelastic collision of an incident photon $\hbar\omega_i$ with a molecule in the initial energy level E_i (Fig. 3.1a). Following the collision, a photon $\hbar\omega_s$ with lower energy is detected and the molecule is found in a higher-energy level E_f

$$\hbar\omega_i + M(E_i) \rightarrow M^*(E_f) + \hbar\omega_s, \quad \text{with} \quad \hbar(\omega_i - \omega_s) = E_f - E_i > 0. \quad (3.1a)$$

The energy difference $\Delta E = E_f - E_i$ may appear as vibrational, rotational, or electronic energy of the molecule.

If the photon $\hbar\omega_i$ is scattered by a vibrationally excited molecule, it may gain energy and the scattered photon has a higher frequency ω_{as} (Fig. 3.1c), where

$$\hbar\omega_{as} = \hbar\omega_i + E_i - E_f, \quad \text{with} \quad E_i > E_f. \quad (3.1b)$$

This “superelastic” photon scattering is called *anti-Stokes radiation*.

In the energy level scheme (Fig. 3.1b), the intermediate state $E_v = E_i + \hbar\omega_i$ of the system “during” the scattering process is often formally described as

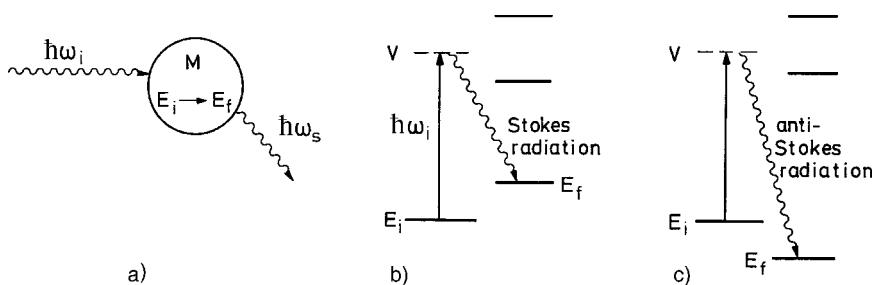


Fig. 3.1a–c. Schematic level diagram of Raman scattering

a *virtual* level, which, however, is not necessarily a “real” stationary eigenstate of the molecule. If the virtual level coincides with one of the molecular eigenstates, one speaks of the *resonance Raman effect*.

A classical description of the *vibrational Raman effect* (which was the main process studied before the introduction of lasers) has been developed by Placek [3.8]. It starts from the relation

$$\mathbf{p} = \boldsymbol{\mu}_0 + \tilde{\alpha} \mathbf{E} , \quad (3.2)$$

between the electric field amplitude $\mathbf{E} = \mathbf{E}_0 \cos \omega t$ of the incident wave and the dipole moment \mathbf{p} of a molecule. The first term $\boldsymbol{\mu}_0$ represents a possible *permanent* dipole moment while $\tilde{\alpha} \mathbf{E}$ is the *induced* dipole moment. The polarizability is generally expressed by the tensor (α_{ij}) of rank two, which depends on the molecular symmetry. Dipole moment and polarizability are functions of the coordinates of the nuclei and electrons. However, as long as the frequency of the incident radiation is far off resonance with electronic or vibrational transitions, the nuclear displacements induced by the polarization of the electron cloud are sufficiently small. Since the electronic charge distribution is determined by the nuclear positions and adjusts “instantaneously” to changes in these positions, we can expand the dipole moment and polarizability into Taylor series in the normal coordinates q_n of the nuclear displacements

$$\begin{aligned} \boldsymbol{\mu} &= \boldsymbol{\mu}(0) + \sum_{n=1}^Q \left(\frac{\partial \boldsymbol{\mu}}{\partial q_n} \right)_0 q_n + \dots , \\ \alpha_{ij}(q) &= \alpha_{ij}(0) + \sum_{n=1}^Q \left(\frac{\partial \alpha_{ij}}{\partial q_n} \right)_0 q_n + \dots , \end{aligned} \quad (3.3)$$

where $Q = 3N - 6$ (or $3N - 5$ for linear molecules) gives the number of normal vibrational modes for a molecule with N nuclei, and $\boldsymbol{\mu}(0) = \boldsymbol{\mu}_0$ and $\alpha_{ij}(0)$ are the dipole moment and the polarizability at the equilibrium configuration $q_n = 0$. For small vibrational amplitudes the normal coordinates $q_n(t)$ of the vibrating molecule can be approximated by

$$q_n(t) = q_{n0} \cos(\omega_n t) , \quad (3.4)$$

where q_{n0} gives the amplitude, and ω_n the vibrational frequency of the n th normal vibration. Inserting (3.4 and 3.3) into (3.2) yields the total dipole moment

$$\begin{aligned} p = \mu_0 + \sum_{n=1}^Q \left(\frac{\partial \mu}{\partial q_n} \right)_0 q_{n0} \cos(\omega_n t) + \alpha_{ij}(0) E_0 \cos(\omega t) \\ + \frac{1}{2} E_0 \sum_{n=1}^Q \left(\frac{\partial \alpha_{ij}}{\partial q_n} \right)_0 q_{n0} [\cos(\omega + \omega_n)t + \cos(\omega - \omega_n)t]. \end{aligned} \quad (3.5)$$

The second term describes the infrared spectrum, the third term the Rayleigh scattering, and the last term represents the Raman scattering. In Fig. 3.2 the dependence of $\partial \mu / \partial q$ and $\partial \alpha / \partial q$ is shown for the three normal vibrations of the CO_2 molecule. This illustrates that $\partial \mu / \partial q \neq 0$ for the bending vibration ν_2 and for the asymmetric stretch ν_3 . These two vibrational modes are called “infrared active.” The polarizability change is $\partial \alpha / \partial q \neq 0$ only for the symmetric stretch ν_1 , which is therefore called “Raman active.”

Since an oscillating dipole moment is a source of new waves generated at each molecule, (3.5) shows that an elastically scattered wave at the frequency ω of the incident wave is produced (Rayleigh scattering) as are inelastically scattered components with the frequencies $\omega - \omega_n$ (*Stokes waves*) and superelastically scattered waves with the frequencies $\omega + \omega_n$ (*anti-Stokes components*). The microscopic contributions from each molecule add up to macroscopic waves with intensities that depend on the population $N(E_i)$ of

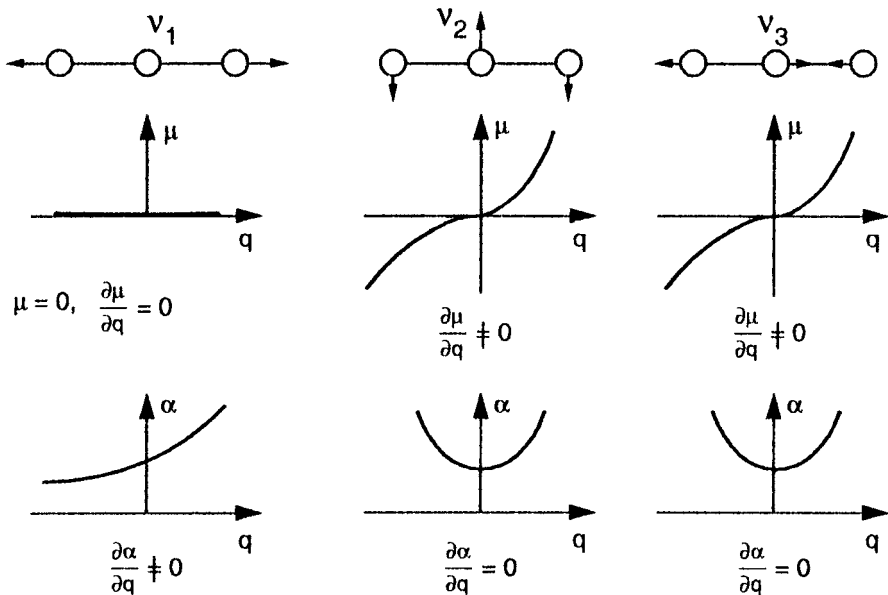


Fig. 3.2. Dependence $\partial \mu / \partial q$ of dipole moment and $\partial \alpha / \partial q$ of polarizability on the normal vibrations of the CO_2 molecule

the molecules in the initial level E_i , on the intensity of the incident radiation, and on the expression $(\partial\alpha_{ij}/\partial q_n)q_n$, which describes the dependence of the polarizability components on the nuclear displacements.

Although the classical theory correctly describes the frequencies $\omega \pm \omega_n$ of the Raman lines, it fails to give the correct intensities and a quantum mechanical treatment is demanded. The expectation value of the component α_{ij} of the polarizability tensor is given by

$$\langle \alpha_{ij} \rangle_{ab} = \int u_b^*(q) \alpha_{ij} u_a(q) dq, \quad (3.6)$$

where the functions $u(q)$ represent the molecular eigenfunctions in the initial level a and the final level b . The integration extends over all nuclear coordinates. This shows that a computation of the intensities of Raman lines is based on the knowledge of the molecular wave functions of the initial and final states. In the case of vibrational-rotational Raman scattering these are the rotational-vibrational eigenfunctions of the electronic ground state.

For small displacements q_n , the molecular potential can be approximated by a harmonic potential, where the coupling between the different normal vibrational modes can be neglected. The functions $u(q)$ are then separable into a product

$$u(q) = \prod_{n=1}^Q w_n(q_n, v_n), \quad (3.7)$$

of vibrational eigenfunction of the n th normal mode with v_n vibrational quanta. Using the orthogonality relation

$$\int w_n w_m dq = \delta_{nm}, \quad (3.8)$$

of the functions $w_n(q_n)$, one obtains from (3.6 and 3.3)

$$\langle \alpha_{ij} \rangle_{ab} = (\alpha_{ij})_0 + \sum_{n=1}^Q \left(\frac{\partial \alpha_{ij}}{\partial q_n} \right)_0 \int w_n(q_n, v_a) q_n w_n(q_n, v_b) dq_n. \quad (3.9)$$

The first term is a constant and is responsible for the Rayleigh scattering. For nondegenerate vibrations the integrals in the second term vanish unless $v_a = v_b \pm 1$. In these cases it has the value $[\frac{1}{2}(v_a + 1)]^{1/2}$ [3.18]. The basic intensity parameter of vibrational Raman spectroscopy is the derivative $(\partial\alpha_{ij}/\partial q)$, which can be determined from the Raman spectra.

The intensity of a Raman line at the Stokes or anti-Stokes frequency $\omega_s = \omega \pm \omega_n$ is determined by the population density $N_i(E_i)$ in the initial level $E_i(v, J)$, by the intensity I_L of the incident pump laser, and by the

Raman scattering cross section $\sigma_R(i \rightarrow f)$ for the Raman transition $E_i \rightarrow E_f$:

$$I_s = N_i(E_i)\sigma_R(i \rightarrow f)I_L. \quad (3.10)$$

At thermal equilibrium the population density $N_i(E_i)$ follows the Boltzmann distribution

$$N_i(E_i, v, J) = \frac{N}{Z} g_i e^{-E_i/kT}, \quad \text{with} \quad N = \sum N_i. \quad (3.11a)$$

The statistical weight factors g_i depend on the vibrational state $v = (n_1 v_1, n_2 v_2, \dots)$, the rotational state with the rotational quantum number J , the projection K onto the symmetry axis in the case of a symmetric top, and furthermore on the nuclear spins I of the N nuclei. The partition function

$$Z = \sum_i g_i e^{-E_i/kT}, \quad (3.11b)$$

is a normalization factor, which makes $\sum N_i(v, J) = N$, as can be verified by inserting (3.11b) into (3.11a).

In case of Stokes radiation the initial state of the molecules may be the vibrational ground state, while for the emission of anti-Stokes lines the molecules must have initial excitation energy. Because of the lower population density in these excited levels, the intensity of the anti-Stokes lines is lower by a factor $\exp(-\hbar\omega_v/kT)$.

Example 3.1.

$\hbar\omega_v = 1000 \text{ cm}^{-1}$, $T = 300 \text{ K} \rightarrow kT \sim 250 \text{ cm}^{-1} \rightarrow \exp(-E_i/kT) \approx e^{-4} \approx 0.018$. With comparable cross sections σ_R the intensity of anti-Stokes lines is therefore lower by two orders of magnitude compared with those of Stokes lines.

The scattering cross section depends on the matrix element (3.9) of the polarizability tensor and furthermore contains the ω^4 frequency dependence derived from the classical theory of light scattering. One obtains [3.19] analogously to the two-photon cross section (Sect. 2.5)

$$\sigma_R(i \rightarrow f) = \frac{8\pi\omega_s^4}{9\hbar c^4} \left| \sum_j \frac{\langle\alpha_{ij}\rangle\hat{\mathbf{e}}_L\langle\alpha_{jf}\rangle\hat{\mathbf{e}}_s}{\omega_{ij} - \omega_L - i\gamma_j} + \frac{\langle\alpha_{ji}\rangle\hat{\mathbf{e}}_L\langle\alpha_{jf}\rangle\hat{\mathbf{e}}_s}{\omega_{jf} - \omega_L - i\gamma_j} \right|^2, \quad (3.12)$$

where $\hat{\mathbf{e}}_L$ and $\hat{\mathbf{e}}_s$ are unit vectors representing the polarization of the incident laser beam and the scattered light. The sum extends over all molecular levels j with homogeneous width γ_j accessible by single-photon transitions from the initial state i . We see from (3.12) that the initial and final states are connected by *two-photon* transitions, which implies that both states have the same parity. For example, the vibrational transitions in homonuclear diatomic molecules, which are forbidden for single-photon infrared transitions, are accessible to Raman transitions.

The matrix elements $\langle\alpha_{ij}\rangle$ depend on the symmetry characteristics of the molecular states. While the theoretical evaluation of the magnitude of $\langle\alpha_{ij}\rangle$ demands a knowledge of the corresponding wave functions, the question whether $\langle\alpha_{ij}\rangle$ is zero or not depends on the symmetry properties of the molecular wave functions for the states $|i\rangle$ and $|f\rangle$ and can therefore be answered by group theory without explicitly calculating the matrix elements (3.9).

According to (3.12), the Raman scattering cross section increases considerably if the laser frequency ω_L matches a transition frequency ω_{ij} of the molecule (resonance Raman effect) [3.20, 3.21]. With tunable dye lasers and optical frequency doubling this resonance condition can often be realized. The enhanced sensitivity of resonant Raman scattering can be utilized for measurements of micro-samples or of very small concentrations of molecules in solutions, where the absorption of the pump wave is small in spite of resonance with a molecular transition.

If the frequency difference $\omega_L - \omega_s$ corresponds to an electronic transition of the molecule, we speak of electronic Raman scattering [3.22, 3.23], which gives complementary information to electronic-absorption spectroscopy. This is because the initial and final states must have the same parity, and therefore a direct dipole-allowed electronic transition $|i\rangle \rightarrow |f\rangle$ is not possible.

In paramagnetic molecules Raman transitions between different fine-structure components (spin-flip Raman transitions) can occur [3.9]. If the molecules are placed in a longitudinal magnetic field parallel to the laser beam, the Raman light is circularly polarized and is measured as σ^+ light for $\Delta M = +1$ and as σ^- for $\Delta M = -1$ transitions.

3.2 Experimental Techniques of Linear Laser Raman Spectroscopy

The scattering cross sections in spontaneous Raman spectroscopy are very small, typically on the order of 10^{-30} cm^2 . The experimental problems of detecting weak signals in the presence of intense background radiation are by no means trivial. The achievable signal-to-noise ratio depends both on the pump intensity and on the sensitivity of the detector. Recent years have brought remarkable progress on the source as well as on the detector side [3.24]. The incident light intensity can be greatly enhanced by using multiple reflection cells, intracavity techniques (Sect. 1.2.2), or a combination of both. Figure 3.3 depicts as an example of such advanced equipment a Raman spectrometer with a multiple-reflection Raman cell inside the resonator of an argon laser. The laser can be tuned by the Brewster prism with reflecting backside (LP + M) to the different laser lines [3.25]. A sophisticated system of mirrors CM collects the scattered light, which is further imaged by the lens L_1 onto the entrance slit S of the spectrometer. A Dove prism DP [3.26] turns the image of the line source by 90° to make it parallel to the entrance slit. Figure 3.4, which shows the pure rotational Raman spectrum of C_2N_2 , illustrates

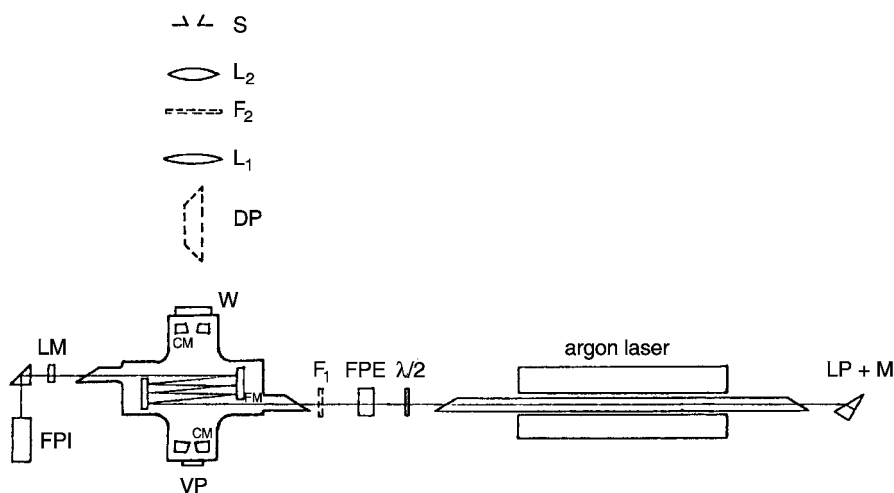


Fig. 3.3. Experimental arrangement for intracavity Raman spectroscopy with an argon laser: CM, multiple reflection four-mirror system for efficient collection of scattered light; LM, laser-resonator mirror; DP, Dove prism, which turns the image of the horizontal interaction plane by 90° in order to match it to the vertical entrance slit S of the spectrograph; FPE, Fabry-Perot etalon to enforce single-mode operation of the argon laser; LP, Littrow prism for line selection [3.25]

the sensitivity that can be obtained with this setup [3.25].

In earlier days of Raman spectroscopy the photographic plate was the only detector used to record the Raman spectra. The introduction of sensitive photomultipliers and, in particular, the development of image intensifiers and optical multichannel analyzers with cooled photocathodes (Vol. 1, Sect. 4.5) have greatly enhanced the detection sensitivity. Image intensifiers and instrumentation such as optical multichannel analyzers (OMAs) or CCD arrays (Vol. 1, Sect. 4.5.3) allow simultaneous recording of extended spectral ranges with sensitivities comparable to those of photomultipliers [3.26].

The third experimental component that has contributed to the further improvement of the quality of Raman spectra is the introduction of digital computers to control the experimental procedure, to calibrate the Raman spec-

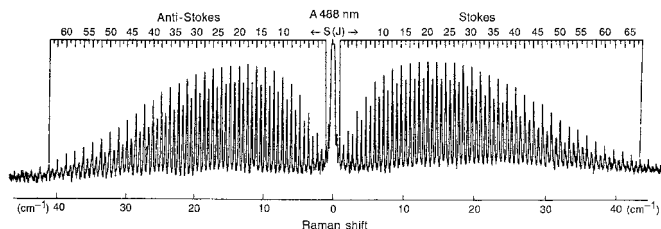


Fig. 3.4. Rotational Raman spectrum of C_2N_2 excited with the 488-nm line of the argon laser in the experimental setup of Fig. 3.3 and recorded on a photographic plate with 10-min exposure time [3.25]

tra, and to analyze the data. This has greatly reduced the time spent for preparing the data for the interpretation of the results [3.27].

Because of the increased sensitivity of an intracavity arrangement, even weak vibrational overtone bands with $\Delta v > 1$ can be recorded with rotational resolution. For illustration, Fig. 3.5 shows the rotationally resolved Q-branch of the D_2 molecule for the transitions ($v' = 2 \leftarrow v'' = 0$) [3.28]. The photon counting rate for the overtone transitions was about 5000 times smaller than those for the fundamental ($v' = 1 \leftarrow v'' = 0$) band. This overtone Raman spectroscopy can also be applied to large molecules, as has been demonstrated for the overtone spectrum of the torsional vibration of CH_3CD_3 and C_2H_6 , where the torsional splittings could be measured up to the 5th torsional level [3.29].

Just as in absorption spectroscopy, the sensitivity may be enhanced by difference laser Raman spectroscopy, where the pump laser passes alternately through a cell containing the sample molecules dissolved in some liquid and through a cell containing only the liquid. The basic advantages of this difference technique are the cancellation of unwanted Raman bands of the solvent in the spectrum of the solution and the accurate determination of small frequency shifts due to interactions with the solvent molecules.

In the case of strongly absorbing Raman samples, the heat production at the focus of the incident laser may become so large that the molecules under investigation may thermally decompose. A solution to this problem is the rotating sample technique [3.30], where the sample is rotated with an angular velocity Ω . If the interaction point with the laser beam is R centimeters away from the axis, the time T spent by the molecules within the focal region with diameter d [cm] is $T = d/(R\Omega)$. This technique which allows much higher input powers and therefore better signal-to-noise ratios,

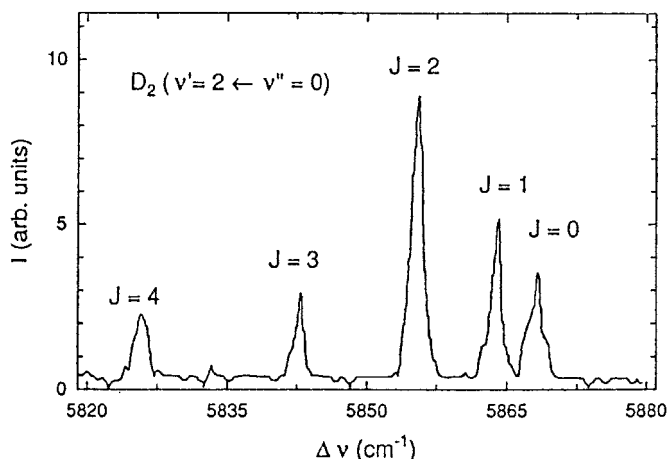


Fig. 3.5. Rotationally resolved Q-branch in the ($v' = 2 \leftarrow v'' = 0$) overtone spectrum of the D_2 molecule, measured with the sample inside the resonator of a 250-W argon laser at $\lambda = 488 \text{ nm}$ [3.28]

can be combined with the difference technique by mounting a cylindrical cell onto the rotation axis. One half of the cell is filled with the liquid Raman sample in solution, the other half is only filled with the solvent (Fig. 3.6).

A larger increase of sensitivity in linear Raman spectroscopy of liquids has been achieved with optical-fiber Raman spectroscopy. This technique uses a capillary optical fiber with the refractive index n_f , filled with a liquid with refractive index $n_e > n_f$. If the incident laser beam is focused into the fiber, the laser light as well as the Raman light is trapped in the core due to internal reflection and therefore travels inside the capillary. With sufficiently long capillaries (1–30 m) and low losses, very high spontaneous Raman intensities can be achieved, which may exceed those of conventional techniques by factors of 10^3 [3.31]. Figure 3.7 shows schematically the experimental arrangement where the fiber is wound on a drum. Because of the increased sensitivity, this fiber technique also allows one to record second- and third-order Raman bands, which facilitates complete assignments of vibrational spectra [3.32].

The sensitivity of Raman spectroscopy in the gas phase can be greatly enhanced by combination with one of the detection techniques discussed

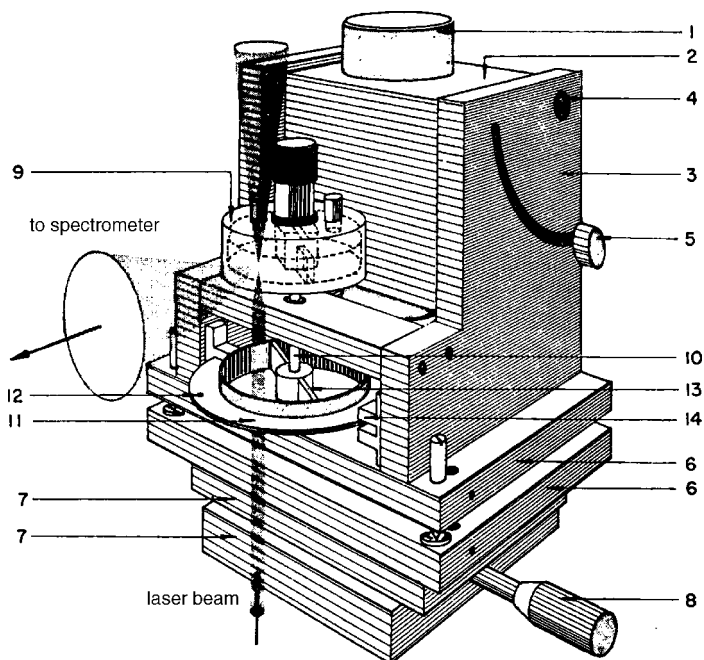


Fig. 3.6. Rotating sample cell used for difference Raman spectroscopy: 1, motor; 2, motor block; 3, side parts; 4, motor axis; 5, set screw; 6, kinematic mount; 7, x-y precision ball glider; 8, adjustment screw; 9, divided liquid cell for difference Raman spectroscopy; 10, axis for trigger wheel; 11, trigger wheel; 12, trigger hole; 13, bar; 14, optoelectronic array consisting of a photodiode and transistor [3.30]

in Chap. 1. For example, the vibrationally excited molecules produced by Raman–Stokes scattering can be selectively detected by resonant two-photon ionization with two visible lasers or by UV ionization with a laser frequency ω_{UV} , which can ionize molecules in level E_f but not in E_i (Fig. 3.8).

The combination of Raman spectroscopy with Fourier-transform spectroscopy [3.33] allows the simultaneous detection of larger spectral ranges in the Raman spectra.

The information obtained from linear Raman spectroscopy is derived from the following experimental data:

- The linewidth of the scattered radiation, which represents for gaseous samples a convolution of the Doppler width, collisional broadening, spectral profile of the exciting laser, and natural linewidth, depending on the lifetimes of molecular levels involved in the Raman transition.

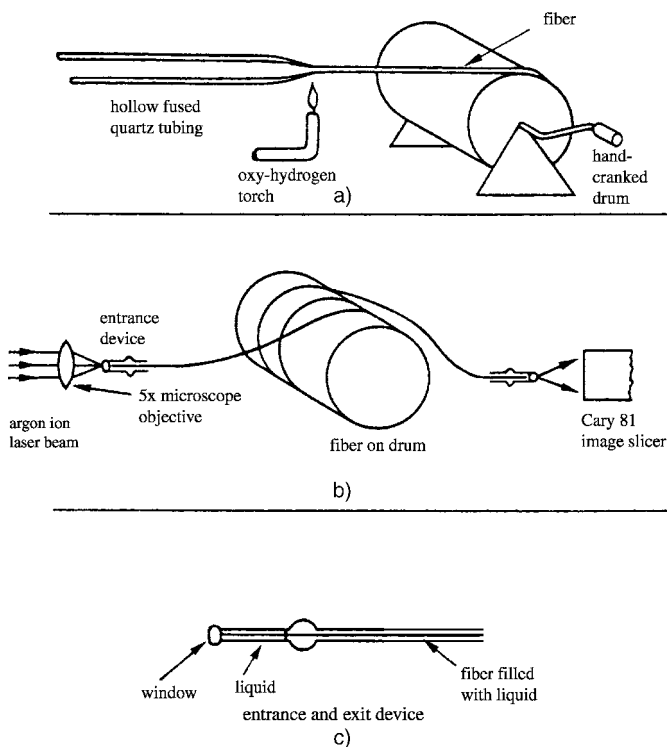


Fig. 3.7a–c. Raman spectroscopy of liquid samples in a thin capillary fiber: (a) production of the fiber; (b) incoupling of an argon laser beam with a microscope objective into the fiber and imaging of the outcoupled radiation into a spectrometer; (c) fiber with liquid [3.30]

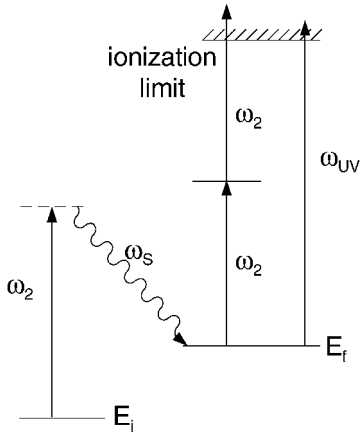


Fig. 3.8. Detection of Raman–Stokes scattering by photoionization of the excited level E_f either by one UV photon ($IP(E_f) < \hbar\omega_{UV} < IP(E_i)$) or by resonant two-photon ionization

- The degree of polarization ρ of the scattered light, defined as

$$\rho = \frac{I_{\parallel} - I_{\perp}}{I_{\parallel} + I_{\perp}}, \quad (3.13)$$

where I_{\parallel} and I_{\perp} are the intensities of the scattered light with a polarization parallel and perpendicular, respectively, to that of a linearly polarized excitation laser. A more detailed calculation shows that for statistically oriented molecules the degree of polarization

$$\rho = \frac{3\beta^2}{45\bar{\alpha}^2 + 4\beta^2}, \quad (3.14)$$

depends on the mean value $\bar{\alpha} = (\alpha_{xx} + \alpha_{yy} + \alpha_{zz})/3$ of the diagonal components of the polarizability tensor $\tilde{\alpha}$ and on the anisotropy

$$\beta^2 = \frac{1}{2} \left[(\alpha_{xx} - \alpha_{yy})^2 + (\alpha_{yy} - \alpha_{zz})^2 + (\alpha_{zz} - \alpha_{xx})^2 + 6(\alpha_{xy}^2 + \alpha_{xz}^2 + \alpha_{zx}^2) \right]. \quad (3.15)$$

Measurements of ρ and β therefore allow the determination of the polarizability tensor [3.34].

It turns out that

$$\begin{aligned} \overline{\alpha_{xx}^2} &= \overline{\alpha_{yy}^2} = \overline{\alpha_{zz}^2} = \frac{1}{45} (45\bar{\alpha}^2 + 4\beta^2), \\ \overline{\alpha_{xy}^2} &= \overline{\alpha_{xz}^2} = \overline{\alpha_{yz}^2} = \frac{1}{15} \beta^2. \end{aligned} \quad (3.16)$$

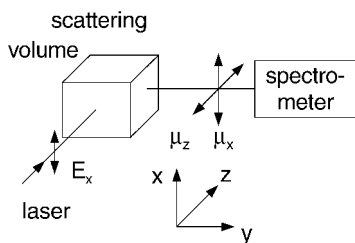


Fig. 3.9. Possible scattering geometry for measurements of the components α_{xx} and α_{zx} of the polarizability tensor

With the experimental arrangement of Fig. 3.9, where the exciting laser is polarized in the x -direction and the Raman light is observed in the y -direction without polarizer ($\mu_x + \mu_z$), the measured intensity becomes

$$I_{x,(x+z)} = \frac{\omega^4 \cdot I_0}{16\pi^2 \epsilon_0^2 c^4} (\alpha_{xx}^2 + \alpha_{zx}^2). \quad (3.17)$$

- The intensity of the Raman lines is proportional to the product of the Raman scattering cross section σ_R , which depends according to (3.12) on the matrix elements $\langle \alpha_{ij} \rangle$ of the polarizability tensor and the density N_i of molecules in the initial state. If the cross sections σ_R have been determined elsewhere, the intensity of the Raman lines can be used for measurements of the population densities $N(v, J)$. Assuming a Boltzmann distribution (3.11a), the temperature T of the sample can be derived from measured values of $N(v, J)$. This is frequently used for the determination of unknown temperature profiles in flames [3.35] or of unknown density profiles in liquid or gaseous flows [3.36] at a known temperature (Sect. 3.5). One example is intracavity Raman spectroscopy of molecules in a supersonic jet, demonstrated by van Helvoort et al. [3.37]. If the intracavity beam waist of an argon-ion laser is shifted to different locations of the molecular jet (Fig. 3.10), the vibrational and rotational temperatures of the molecules (Sect. 4.2) and their local variations can be derived from the Raman spectra.

More details of recent techniques in linear laser Raman spectroscopy can be found in [3.11, 3.38].

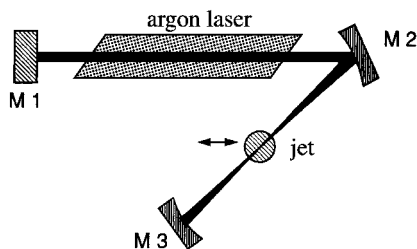


Fig. 3.10. Intracavity Raman spectroscopy of molecules in a cold jet with spatial resolution

3.3 Nonlinear Raman Spectroscopy

When the intensity of the incident light wave becomes sufficiently large, the induced oscillation of the electron cloud surpasses the linear range assumed in Sect. 3.1. This implies that the induced dipole moments \mathbf{p} of the molecules are no longer proportional to the electric field \mathbf{E} and we have to generalize (3.2). The function $\mathbf{p}(\mathbf{E})$ can be expanded into a power series of E^n ($n = 0, 1, 2, \dots$), which is generally written as

$$\mathbf{p}(\mathbf{E}) = \boldsymbol{\mu} + \tilde{\alpha}\mathbf{E} + \tilde{\beta}\mathbf{E} \cdot \mathbf{E} + \tilde{\gamma}\mathbf{E} \cdot \mathbf{E} \cdot \mathbf{E}, \quad (3.18a)$$

where $\tilde{\alpha}$ is the polarizability tensor, $\tilde{\beta}$ is named *hyper-polarizability*, and $\tilde{\gamma}$ is called the *second hyper-polarizability*. The quantities α , β , and γ are tensors of rank two, three, and four, respectively.

In component notation ($i = x, y, z$) (3.18a) can be written as

$$\begin{aligned} p_i(\mathbf{E}) = & \mu_i + \sum_k \alpha_{ik} E_k + \sum_k \sum_j \beta_{ikj} E_k E_j \\ & + \sum_k \sum_j \sum_l \gamma_{ikjl} E_k E_j E_l. \end{aligned} \quad (3.18b)$$

This gives for the polarization $\mathbf{P} = N\mathbf{p}$ of a medium with N oriented dipoles

$$P_i(\mathbf{E}) = \epsilon_0 \left(\chi_i + \sum_k \chi_{ik} E_k + \sum_{k,j} \chi_{ikj} E_k E_j + \dots \right), \quad (3.18c)$$

which corresponds to Vol. 1, (5.114) discussed in the section on nonlinear optics and frequency conversion, if we define the susceptibilities $\chi_i = N\mu_i/\epsilon_0$, $\chi_{ik} = N\alpha_{ik}/\epsilon_0$, and so on.

For sufficiently small electric field amplitudes E the nonlinear terms in (3.18a) can be neglected, and we then obtain (3.2) for the linear Raman spectroscopy.

3.3.1 Stimulated Raman Scattering

If the incident laser intensity I_L becomes very large, an appreciable fraction of the molecules in the initial state E_i is excited into the final state E_f and the intensity of the Raman-scattered light is correspondingly large. Under these conditions we have to consider the simultaneous interaction of the molecules with *two* EM waves: the laser wave at the frequency ω_L and the Stokes wave at the frequency $\omega_S = \omega_L - \omega_V$ or the anti-Stokes wave at $\omega_a = \omega_L + \omega_V$. Both waves are coupled by the molecules vibrating with the frequencies ω_V . This parametric interaction leads to an energy exchange between the pump wave and the Stokes or anti-Stokes waves. This phenomenon of *stimulated* Raman scattering, which was first observed by Woodbury et al. [3.39] and then explained by Woodbury and Eckhardt [3.40], can be described in classical terms [3.41, 3.42].

The Raman medium is taken as consisting of N harmonic oscillators per unit volume, which are independent of each other. Because of the combined action of the incident laser wave and the Stokes wave, the oscillators experience a driving force \mathbf{F} that depends on the total field amplitude \mathbf{E}

$$\mathbf{E}(z, t) = \mathbf{E}_L e^{i(\omega_L t - k_L z)} + \mathbf{E}_S e^{i(\omega_S t - k_S z)}, \quad (3.19)$$

where we have assumed plane waves traveling in the z -direction. The potential energy W_{pot} of a molecule with induced dipole moment $\mathbf{p} = \alpha \mathbf{E}$ in an EM field with amplitude \mathbf{E} is, according to (3.2, 3.3) with $\mu = 0$

$$W_{\text{pot}} = -\mathbf{p} \cdot \mathbf{E} = -\alpha(q) E^2. \quad (3.20)$$

The force $\mathbf{F} = -\text{grad } W_{\text{pot}}$ acting on the molecule gives

$$\mathbf{F}(z, t) = + \frac{\partial}{\partial q} \{ [\alpha(q)] E^2 \} = \left(\frac{\partial \alpha}{\partial q} \right)_0 E^2(z, t). \quad (3.21)$$

The equation of motion for the molecular oscillator with oscillation amplitude q , mass m , and vibrational eigenfrequency ω_v is then

$$\frac{\partial^2 q}{\partial t^2} - \gamma \frac{\partial q}{\partial t} + \omega_v^2 q = \left(\frac{\partial \alpha}{\partial q} \right)_0 E^2/m, \quad (3.22)$$

where γ is the damping constant that is responsible for the linewidth $\Delta\omega = \gamma$ of spontaneous Raman scattering. Inserting the complex ansatz

$$q = \frac{1}{2} (q_v e^{i\omega t} + q_v^* e^{-i\omega t}), \quad (3.23)$$

into (3.22) we get with the field amplitude (3.19)

$$(\omega_v^2 - \omega^2 + i\gamma\omega) q_v e^{i\omega t} = \frac{1}{2m} \left(\frac{\partial \alpha}{\partial q} \right)_0 E_L E_S e^{i[(\omega_L - \omega_S)t - (k_L - k_S)z]}. \quad (3.24)$$

Comparison of the time-dependent terms on both sides of (3.24) shows that $\omega = \omega_L - \omega_S$. The molecular vibrations are therefore driven at the difference frequency $\omega_v = \omega_L - \omega_S$. Solving (3.24) for q_v yields

$$q_v = \frac{(\partial \alpha / \partial q)_0 E_L E_S}{2m[\omega_v^2 - (\omega_L - \omega_S)^2 + i(\omega_L - \omega_S)\gamma]} e^{-i(k_L - k_S)z}. \quad (3.25)$$

The induced oscillating molecular dipoles $\mathbf{p}(\omega, z, t)$ result in a macroscopic polarization $\mathbf{P} = N\mathbf{p}$. According to (3.5), the polarization $P_S = P(\omega_S)$ at the Stokes frequency ω_S , which is responsible for Raman scattering, is given by

$$P_S = \frac{1}{2} N \left(\frac{\partial \alpha}{\partial q} \right)_0 q E. \quad (3.26)$$

Inserting q from (3.23, 3.25) and E from (3.19) yields the *nonlinear* polarization

$$P_S^{\text{NL}}(\omega_S) = N \frac{(\partial\alpha/\partial q)_0^2 E_L^2 E_S}{4m[\omega_v^2 - (\omega_L - \omega_S)^2 + i\gamma(\omega_L - \omega_S)]} e^{-i(\omega_S t - k_S z)}. \quad (3.27)$$

This shows that a *polarization wave* travels through the medium with an amplitude proportional to the product $E_L^2 \cdot E_S$. It has the same wave vector k_S as the Stokes wave and can therefore amplify this wave. The amplification can be derived from the wave equation

$$\Delta E = \mu_0 \sigma \frac{\partial}{\partial t} E + \mu_0 \epsilon \frac{\partial^2}{\partial t^2} E + \mu_0 \frac{\partial^2}{\partial t^2} (P_S^{\text{NL}}), \quad (3.28)$$

for waves in a medium with the conductivity σ , where P_S^{NL} acts as the driving term.

For the one-dimensional problem ($\partial/\partial y = \partial/\partial x = 0$) with the approximation $d^2 E/dz^2 \ll k dE/dz$ and with (3.26), the equation for the Stokes wave becomes

$$\frac{dE_S}{dz} = -\frac{\sigma}{2} \sqrt{\mu_0/\epsilon} E_S + N \frac{k_S}{2\epsilon} \left(\frac{\partial\alpha}{\partial q} \right)_0 q_v E_L. \quad (3.29)$$

Substituting q_v from (3.25) gives the final result for the case $\omega_v = \omega_L - \omega_S$

$$\frac{dE_S}{dz} = \left[-\frac{\sigma}{2} \sqrt{\mu_0/\epsilon} + N \frac{(\partial\alpha/\partial q)_0^2 E_L^2}{4m\epsilon i\gamma(\omega_L - \omega_S)} \right] E_S = (-f + g) E_S. \quad (3.30)$$

Integration of (3.30) yields

$$E_S = E_S(0) e^{(g-f)z}. \quad (3.31a)$$

The Stokes wave is amplified if the gain g exceeds the losses f . The amplification factor g depends on the square of the laser amplitude E_L and on the term $(\partial\alpha/\partial q)_0^2$. Stimulated Raman scattering is therefore observed only if the incident laser intensity exceeds a threshold value that is determined by the nonlinear term $(\partial\alpha_{ij}/\partial q)_0$ in the polarization tensor of the Raman-active normal vibration and by the loss factor $f = \frac{1}{2}\sigma(\mu_0/\epsilon)^{1/2}$.

According to (3.31), the Stokes intensity increases exponentially with the length z of the interaction zone. If, however, the pump wave is absorbed by the medium, the pump intensity at the position z decreases to

$$I_L(z) = I_L(0) \cdot e^{-\alpha \cdot z}$$

and therefore the gain factor g in (3.30) is smaller. There is an effective length $z = L_{\text{eff}}$ for the optimum intensity I_S of the Stokes wave, which is given by

$$L_{\text{eff}} = (1/\alpha_L)[1 - e^{-\alpha \cdot L}]$$

and the amplitude of the Stokes wave becomes for a medium with length L

$$E_s = E_s(0) \cdot e^{(g \cdot L_{\text{eff}} - f \cdot L)} . \quad (3.31b)$$

While the intensity of anti-Stokes radiation is very small in spontaneous Raman scattering due to the low thermal population density in excited molecular levels (Sect. 3.1), this is not necessarily true in stimulated Raman scattering. Because of the strong incident pump wave, a large fraction of all interacting molecules is excited into higher vibrational levels, and strong anti-Stokes radiation at frequencies $\omega_L + \omega_v$ has been found.

According to (3.26), the driving term in the wave equation (3.28) for an anti-Stokes wave at $\omega_a = \omega_L + \omega_v$ is given by

$$P_{\omega_a}^{\text{NL}} = \frac{1}{2} N \left(\frac{\partial \alpha}{\partial q} \right)_0 q_v E_L e^{i[(\omega_L + \omega_v)t - k_L z]} , \quad (3.32)$$

For small amplitudes $E_a \ll E_L$ of the anti-Stokes waves, we can assume that the molecular vibrations are independent of E_a and can replace q_v by its solution (3.25). This yields an equation for the amplification of E_a that is analogous to (3.29) for E_s

$$\begin{aligned} \frac{dE_a}{dz} = & -\frac{f}{2} E_a e^{i(\omega_a t - k_a z)} \\ & + N_v \left[\frac{\omega_a \sqrt{\mu_0 / \epsilon}}{8m_v} \left(\frac{\partial \alpha}{\partial q} \right)_0^2 \right] E_L^2 E_s^* e^{i(2k_L - k_s - k_a)z} , \end{aligned} \quad (3.33)$$

where N_v is the density of vibrationally excited molecules. This shows that, analogously to sum- or difference-frequency generation (Vol. 1, Sect. 5.8), a macroscopic wave can build up only if the phase-matching condition

$$k_a = 2k_L - k_s , \quad (3.34)$$

can be satisfied. In a medium with normal dispersion this condition cannot be met for collinear waves. From a three-dimensional analysis, however, one obtains the vector equation

$$2\mathbf{k}_L = \mathbf{k}_s + \mathbf{k}_a , \quad (3.35)$$

which reveals that the anti-Stokes radiation is emitted into a cone whose axis is parallel to the beam-propagation direction (Fig. 3.11). The apex angle β of this cone is obtained by multiplying (3.35) with \mathbf{k}_a

$$2\mathbf{k}_L \cdot \mathbf{k}_a = 2k_L k_a \cos \beta = \mathbf{k}_s \cdot \mathbf{k}_a \cos \alpha + k_a^2 . \quad (3.36a)$$

With $k = n \cdot \omega / c$ this can be written as

$$\cos \beta = \frac{n(\omega_s) \omega_s \cos \alpha + n(\omega_a) \omega_a}{2n(\omega_L) \omega_L} . \quad (3.36b)$$

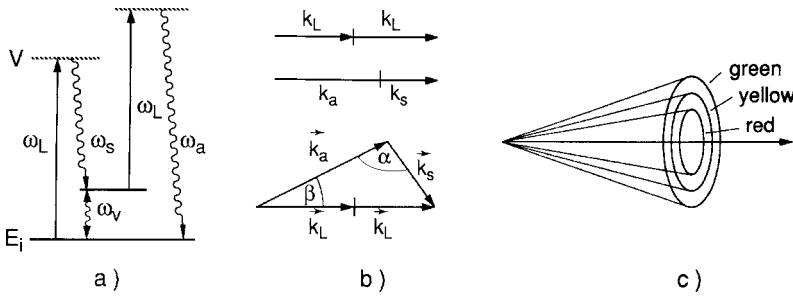


Fig. 3.11a-c. Generation of stimulated anti-Stokes radiation: (a) term diagram illustrating energy conservation; (b) vector diagram of momentum conservation for the collinear and noncollinear case; (c) radiation cone for different values of k_s showing red, yellow, and green rings of anti-Stokes radiation excited by a ruby laser at 694 nm

For $n(\omega_s) = n(\omega_a) = n(\omega_L)$ the collinear case can be realized ($\alpha = \beta = 0$). This is exactly what has been observed [3.39, 3.42].

Let us briefly summarize the differences between the linear (spontaneous) and the nonlinear (induced) Raman effect:

- While the intensity of spontaneous Raman lines is proportional to the incident pump intensity, but lower by several orders of magnitude compared with the pump intensity, the stimulated Stokes or anti-Stokes radiation depend in a nonlinear way on I_p but have intensities comparable to that of the pump wave.
- The stimulated Raman effect is observed only above a threshold pump intensity, which depends on the gain of the Raman medium and the length of the pump region.
- Most Raman-active substances show only one or two Stokes lines at the frequencies $\omega_s = \omega_L - \omega_v$ in stimulated emission. At higher pump intensities, however, lines at the frequencies $\omega = \omega_L - n\omega_v$ ($n = 1, 2, 3$), which do not correspond to overtones of vibrational frequencies, have been observed besides these Stokes lines. Because of the anharmonicity of molecular vibrations, the vibrational levels in an unharmonic potential have energies $E_v = \hbar\omega_v(n + \frac{1}{2}) - x_k\hbar(n + \frac{1}{2})^2$ and therefore the spontaneous Raman lines from vibrational overtones are shifted against ω_L by $\Delta\omega = n\omega_v - (n^2 + n)x_k$, where x_k represent the anharmonicity constants. In Fig. 3.12 is illustrated that these higher-order Stokes lines are generated by consecutive Raman processes, induced by the pump wave, the Stokes wave, etc.
- The linewidths of spontaneous and stimulated Raman lines depend on the linewidth of the pump laser. For narrow linewidths, however, the width of the stimulated Raman lines becomes smaller than that of the spontaneous lines, which are Doppler-broadened by the thermal motion of the scattering molecules. A Stokes photon $\hbar\omega_s$, which is scattered into an angle ϕ against the incident laser beam by a molecule moving with the velocity v ,

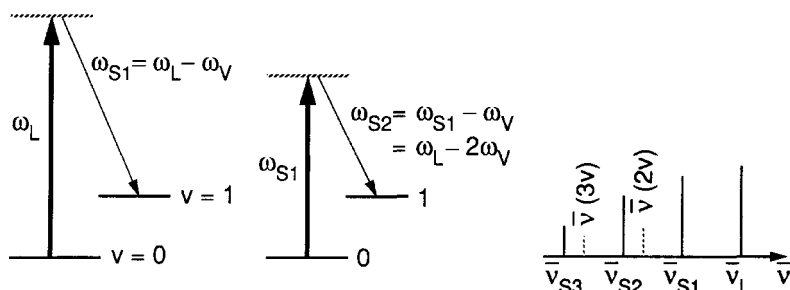


Fig. 3.12. Level diagram for the generation of higher-order Stokes sidebands, which differ from the vibrational overtone frequencies

has a Doppler-shifted frequency

$$\begin{aligned}\omega_s &= \omega_L - \omega_V - (\mathbf{k}_L - \mathbf{k}_S) \cdot \mathbf{v} \\ &= \omega_L - \omega_V - [1 - (k_S/k_L) \cos \phi] \mathbf{k}_L \cdot \mathbf{v}.\end{aligned}\quad (3.37)$$

In the case of spontaneous Raman scattering we have $0 \leq \phi \leq 2\pi$, and the spontaneous Raman lines show a Doppler width that is $(k_S/k_L) = (\omega_S/\omega_L)$ times that of fluorescence lines at ω_L . For induced Raman scattering $\mathbf{k}_S \parallel \mathbf{k}_L \rightarrow \cos \phi = 1$, and the bracket in (3.37) has the value $(1 - k_S/k_L) \ll 1$, if $\omega_V \ll \omega_L$.

- The main merit of the stimulated Raman effect for molecular spectroscopy may be seen in the much higher intensities of stimulated Raman lines. During the same measuring time one therefore achieves a much better signal-to-noise ratio than in linear Raman spectroscopy. The experimental realization of stimulated Raman spectroscopy is based on two different techniques:
 - (a) Stimulated Raman gain spectroscopy (SRGS), where a strong pump laser at ω_L is used to produce sufficient gain for the Stokes radiation at ω_S according to (3.31). This gain can be measured with a weak tunable probe laser tuned to the Stokes wavelengths [3.43] (Fig. 3.13).
 - (b) Inverse Raman spectroscopy (IRS), where the attenuation of the weak probe laser at ω_1 is measured when the strong pump laser at ω_2 is tuned through Stokes or anti-Stokes transitions [3.44].

Several high-resolution stimulated Raman spectrometers have been built [3.43–3.45] that are used for measurements of linewidths and Raman line positions in order to gain information on molecular structure and dynamics. A good compromise for obtaining a high resolution and a large signal-to-noise ratio is to use a pulsed pump laser and a single-mode cw probe laser (quasi-cw spectrometer [3.45]). The narrow-band pulsed laser can be realized by pulsed amplification of a single-mode cw laser (Vol. 1, Sect. 5.7). For illustration Fig. 3.13 shows a typical quasi-cw stimulated Raman spectrometer,

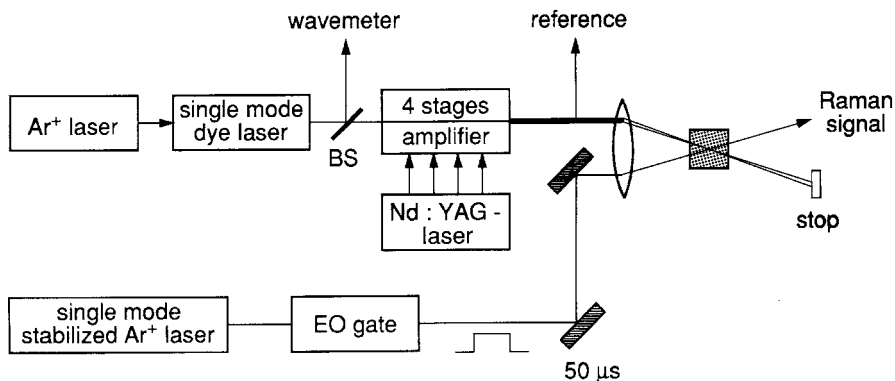


Fig. 3.13. Schematic diagram of a stimulated Raman spectrometer with pulsed, amplified cw pump laser and a single-mode cw probe laser [3.47]

where the wavelengths of the tunable dye laser are measured with a traveling Michelson wavemeter (Vol. 1, Sect. 4.4)

There is another important application of stimulated Raman scattering in the field of *Raman lasers*. With a tunable pump laser at the frequency ω_L , intense coherent radiation sources at frequencies $\omega_L \pm n\omega_V$ ($n = 1, 2, 3, \dots$) can be realized that cover the UV and infrared spectral range if visible pump lasers are used (Vol. 1, Sect. 5.8).

More details on the stimulated Raman effect and reference to experiments in this field can be found in [3.11, 3.46–3.52].

3.3.2 Coherent Anti-Stokes Raman Spectroscopy

In Sect. 3.3.1 we discussed the observation that a sufficiently strong incident pump wave at the frequency ω_L can generate an intense Stokes wave at $\omega_S = \omega_L - \omega_V$. Under the combined action of both waves, the nonlinear polarization P_{NL} of the medium is generated that contains contributions at the frequencies $\omega_V = \omega_L - \omega_S$, $\omega_S = \omega_L - \omega_V$, and $\omega_a = \omega_L + \omega_V$. These contributions act as driving forces for the generation of new waves. Provided that the phase-matching conditions $2\mathbf{k}_L = \mathbf{k}_S + \mathbf{k}_a$ can be satisfied, a strong anti-Stokes wave $E_a \cos(\omega_a t - \mathbf{k}_a \cdot \mathbf{r})$ is observed in the direction of \mathbf{k}_a .

Despite the enormous intensities of stimulated Stokes and anti-Stokes waves, stimulated Raman spectroscopy has been of little use in molecular spectroscopy. The high threshold, which, according to (3.30), depends on the molecular density N , the incident intensity $I \propto E_L^2$, and the square of the small polarizability term $(\partial\alpha_{ij}/\partial q)$ in (3.27), limits stimulated emission to only the strongest Raman lines in materials of high densities N .

The recently developed technique of coherent anti-Stokes Raman spectroscopy (CARS), however, combines the advantages of signal strength obtained in stimulated Raman spectroscopy with the general applicability of

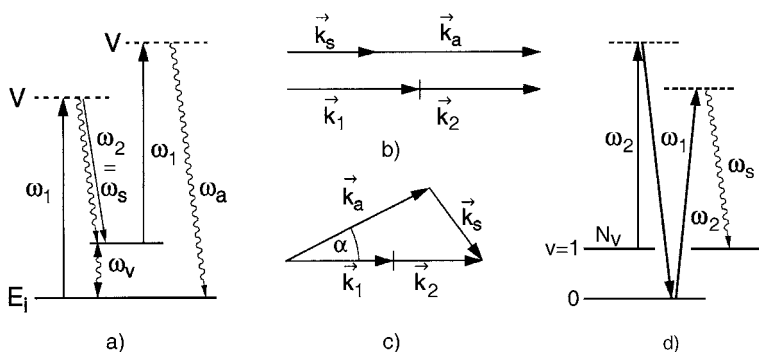


Fig. 3.14. (a) Level diagram of CARS; (b) vector diagrams for phase matching in gases with negligible dispersion and (c) in liquids or solids with noticeable dispersion; (d) generation of coherent Stokes radiation at $\omega_s = 2\omega_2 - \omega_1$

spontaneous Raman spectroscopy [3.46–3.57]. In this technique *two* lasers are needed. The frequencies ω_1 and ω_2 of the two incident laser waves are chosen such that their difference $\omega_1 - \omega_2 = \omega_v$ coincides with a Raman-active vibration of the molecules under investigation. These two incident waves correspond to the pump wave ($\omega_1 = \omega_L$) and the Stokes wave ($\omega_2 = \omega_S$) in stimulated Raman scattering. The advantage is that the Stokes wave at ω_2 is already present and does not need to be generated in the medium. These two waves are considered in (3.19).

Because of the nonlinear interaction discussed in Sect. 3.3.1, new Stokes and anti-Stokes waves are generated (Fig. 3.14d). The waves ω_1 and ω_2 produce a large population density of vibrationally excited molecules by stimulated Raman scattering. These excited molecules act as the nonlinear medium for the generation of anti-Stokes radiation at $\omega_a = 2\omega_1 - \omega_2$ by the incident wave with frequency ω_1 . In a similar way, a Stokes wave with frequency $\omega_s = 2\omega_2 - \omega_1$ is generated by the incident waves at ω_1 and ω_2 (Fig. 3.14d). Since four waves are involved in the generation of the anti-Stokes wave, CARS is called a *four-wave parametric mixing process* (Fig. 3.15).

It can be derived from (3.33) that the power S of the CARS signal (which is proportional to the square of the amplitude E_a)

$$S \propto N^2 I_1^2 I_2, \quad (3.38)$$

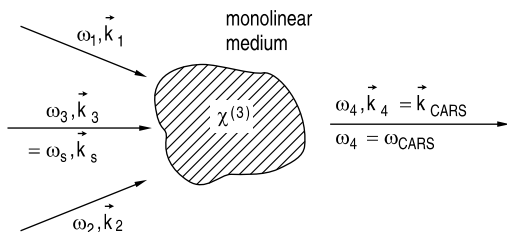


Fig. 3.15. CARS as a four-wave mixing process

increases with the square N^2 of the molecular density N and is proportional to the product $I_1(\omega_1)^2 I_2(\omega_2)$ of the pump laser intensities. It is therefore necessary to use either high densities N or large intensities I . If the two pump beams are focused into the sample, most of the CARS signal is generated within the local volume where the intensities are maximum. CARS spectroscopy therefore offers high spatial resolution.

If the incident waves are at *optical* frequencies, the difference frequency $\omega_R = \omega_1 - \omega_2$ is small compared with ω_1 in the case of rotational–vibrational frequencies ω_R . In gaseous Raman samples the dispersion is generally negligible over small ranges $\Delta\omega = \omega_1 - \omega_2$ and satisfactory phase matching is obtained for *collinear* beams. The Stokes wave at $\omega_S = 2\omega_2 - \omega_1$ and the anti-Stokes wave at $\omega_a = 2\omega_1 - \omega_2$ are then generated in the same direction as the incoming beams (Fig. 3.14b). In liquids, dispersion effects are more severe and the phase-matching condition can be satisfied over a sufficiently long coherence length only, if the two incoming beams are crossed at the phase-matching angle (Fig. 3.14c).

In the collinear arrangement the anti-Stokes wave at $\omega_a = 2\omega_1 - \omega_2$ ($\omega_a > \omega_1$!) is detected through filters that reject both incident laser beams as well as the fluorescence that may be generated in the sample. Figure 3.16 illustrates an early experimental setup used for rotational–vibrational spectroscopy of gases by CARS [3.58]. The two incident laser beams are provided by a Q-switched ruby laser and a tunable dye laser that was pumped by this ruby laser. Because the gain of the anti-Stokes wave depends quadratically on the molecular density N (see (3.38)), megawatt-range power levels of the incident beams are required for gaseous samples, while kilowatt powers are sufficient for liquid samples [3.59].

The most common pump system for pulsed CARS experiments are two dye lasers pumped by the same pump laser (N₂ laser, excimer laser, or frequency-doubled Nd:YAG laser). This system is very flexible because both frequencies ω_1 and ω_2 can be varied over large spectral ranges. Since both the frequency and intensity fluctuations of the dye lasers result in strong intensity

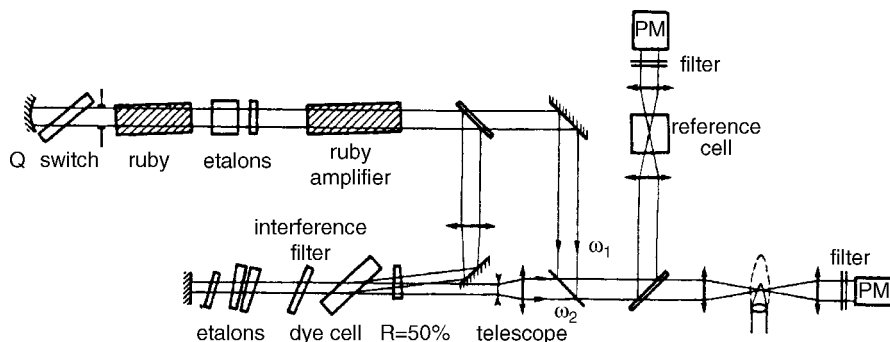


Fig. 3.16. Experimental setup of an early CARS experiment in gases using a ruby laser and a dye laser pumped by the ruby laser [3.58]

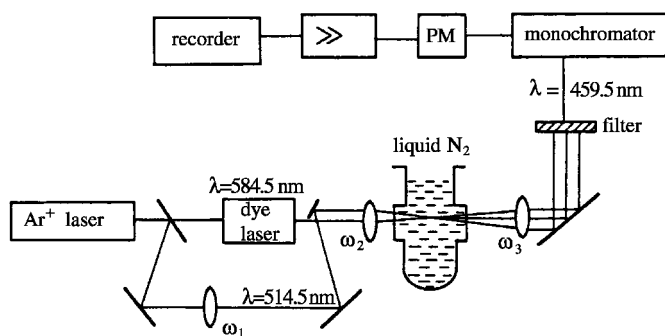


Fig. 3.17. Experimental setup for cw CARS in liquids [3.59]

fluctuations of the CARS signal, the stability of the dye lasers needs particular attention. With compact and stable systems the signal fluctuations can be reduced below 10% [3.60].

In addition, many CARS experiments have been performed with cw dye lasers with liquid samples as well as with gaseous ones. An experimental setup for cw CARS of liquid nitrogen is shown in Fig. 3.17, where the two incident collinear pump waves are provided by the 514.5-nm argon laser line (ω_1) and a cw dye laser (ω_2) pumped by the same argon laser [3.59].

The advantage of cw CARS is its higher spectral resolution because the bandwidth $\Delta\nu$ of single-mode cw lasers is several orders of magnitude below that of pulsed lasers. In order to obtain sufficiently high intensities, intracavity excitation has been used. A possible experimental realization (Fig. 3.18) places the sample cell inside the ring resonator of an argon ion laser, where the cw dye laser is coupled into the resonator by means of a prism [3.44].

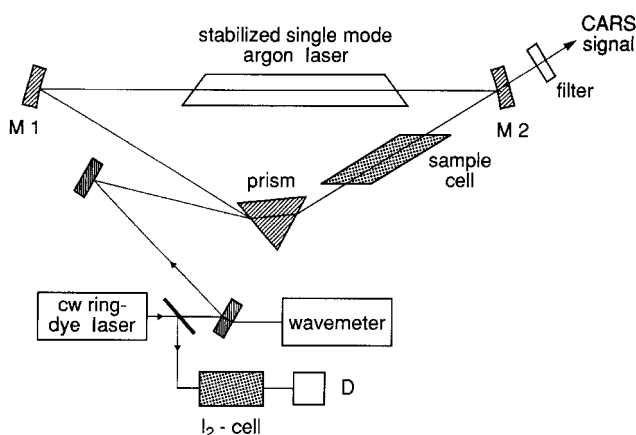


Fig. 3.18. Schematic arrangement of a cw CARS spectrometer with intracavity excitation of the sample [3.44]

The CARS signal generated in the sample cell at the beam waist of the resonator is transmitted through the dichroic mirror M2 and is spectrally purified by a filter or a prism and a monochromator before it reaches a photomultiplier.

High-resolution CARS can be also performed with injection-seeded pulsed dye lasers [3.44, 3.61]. If the radiation of a single-mode cw dye laser with frequency ω is injected into the cavity of a pulsed dye laser that has been mode matched to the Gaussian beam of the cw laser (Vol. 1, Sect. 5.8), the amplification of the gain medium is enhanced considerably at the frequency ω and the pulsed laser oscillates on a single cavity mode at the frequency ω . Only some milliwatts of the cw laser are needed for injection, while the output of the single-mode pulsed laser reaches several kilowatts, which may be further amplified (Vol. 1, Sect. 5.5). Its bandwidth $\Delta\nu$ for pulses of duration Δt is only limited by the Fourier limit $\Delta\nu = 1/(2\pi\Delta t)$.

3.3.3 Resonant CARS and BOX CARS

If the frequencies ω_1 and ω_2 of the two incident laser waves are chosen to match a molecular transition, one or even two of the virtual levels in Fig. 3.14 coincide with a real molecular level. In this case of *resonant CARS*, the sensitivity may be increased by several orders of magnitude. Because of the larger absorption of the incident waves, the absorption path length must be sufficiently short or the density of absorbing molecules must be correspondingly small [3.62, 3.63].

A certain disadvantage of collinear CARS in gases is the spatial overlap of the two parallel incident beams with the signal beam. This overlap must be separated by spectral filters. This disadvantage can be overcome by the BOX CARS technique [3.64], where the pump beam of laser L1 (\mathbf{k}_1, ω_1) is split into two parallel beams that are focused by a lens into the sample (Fig. 3.19b), where the directions of the three incoming beams match the vector diagram of Fig. 3.19a. The CARS signal beam can now be separated by geometrical means (beam stop and apertures). For comparison the vector diagrams of the phase-matching condition (3.35) are shown in Fig. 3.20 for the general case ($\mathbf{k}_1 \neq \mathbf{k}_2$), the collinear CARS arrangement, and for BOX CARS, where the vector diagram has the form of a box. From Fig. 3.19a with the relation $|\mathbf{k}| = n \cdot \omega/c$, the phase-matching conditions

$$\begin{aligned} n_2\omega_2 \sin \theta &= n_3\omega_3 \sin \varphi, \\ n_2\omega_2 \cos \theta + n_3\omega_3 \cos \varphi &= 2n_1\omega_1 \cos \alpha, \end{aligned} \quad (3.39)$$

can be derived, which yield for $\theta = \alpha$ the relation

$$\sin \varphi = \frac{n_2\omega_2}{n_3\omega_3} \sin \alpha, \quad (3.40)$$

between the angle φ of the CARS signal beam $\mathbf{k}_a = \mathbf{k}_3$ against the z -direction and the angle α of the incident beams.

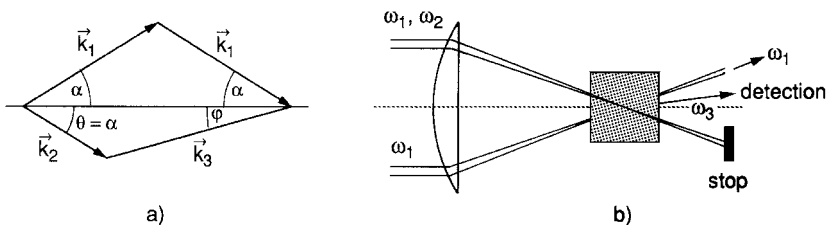


Fig. 3.19a,b. Wave vector diagram for BOX CARS (a) and experimental realization (b)

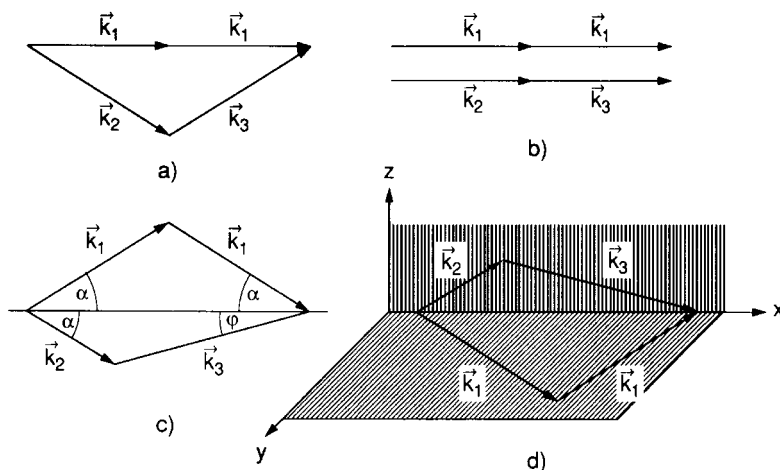


Fig. 3.20a-d. Comparison of phase-matching diagrams for CARS: (a) for the general case $\vec{k}_1 \nparallel \vec{k}_2$; (b) the collinear case $\vec{k}_1 \parallel \vec{k}_2$; (c) for BOX CARS; and (d) for folded BOX CARS

The CARS signal is generated within the common overlap volume of the three incident beams. This BOX-CAR technique considerably increases the spatial resolution, which may reach values below 1 mm.

In another beam configuration (folded BOX CARS), the pump beam with ω_2 is split into two parallel beams, which are directed by the focusing lens in such a way that the wave vectors \vec{k}_2 and $\vec{k}_3 = \vec{k}_{as}$ are contained in a plane orthogonal to that of the two \vec{k}_1 vectors (Fig. 3.20d). This has the advantage that neither of the two pump beams overlaps the signal beam at the detector [3.65]. If the Raman shifts are small, spectral filtering becomes difficult and the advantage of this folded BOX CAR technique is obvious.

The advantages of CARS may be summarized as follows:

- The signal levels in CARS may exceed those obtained in spontaneous Raman spectroscopy by a factor of $10^4 - 10^5$.
- The higher frequency $\omega_3 > \omega_1, \omega_2$ of the anti-Stokes waves allows one to use filters that reject the incident light as well as fluorescence light.
- The small beam divergence allows one to place the detector far away from the sample, which yields excellent spatial discrimination against

fluorescence or thermal luminous background such as occurs in flames, discharges, or chemiluminescent samples.

- The main contribution to the anti-Stokes generation comes from a small volume around the focus of the two incident beams. Therefore very small sample quantities (microliters for liquid samples or millibar pressures for gaseous samples) are required. Furthermore, a high spatial resolution is possible, which allows one to probe the spatial distribution of molecules in definite rotational–vibrational levels. The measurements of local temperature variations in flames from the intensity of anti-Stokes lines in CARS is an example where this advantage is utilized.
- The high spatial resolution is utilized in CARS microscopy, which is mainly applied to the investigation of biological cells and their compositions (see Sect. 3.4.3).
- A high spectral resolution can be achieved without using a monochromator. The Doppler width $\Delta\omega_D$, which represents a principal limitation in 90° spontaneous Raman scattering, is reduced to $[(\omega_2 - \omega_1)/\omega_1]\Delta\omega_D$ for the collinear arrangement used in CARS. While a resolution of 0.3 to 0.03 cm^{-1} is readily obtained in CARS with pulsed lasers, even linewidths down to 0.001 cm^{-1} have been achieved with single-mode lasers.

The main disadvantages of CARS are the expensive equipment and strong fluctuations of the signals caused by instabilities of intensities and alignments of the incident laser beams. The sensitivity of detecting low relative concentrations of specified sample molecules is mainly limited by interference with the nonresonant background from the other molecules in the sample. This limitation can be overcome, however, by resonant CARS.

3.3.4 Hyper-Raman Effect

The higher-order terms $\beta E E$, $\gamma E E E$ in the expansion (3.18a) of $p(E)$ represent the hyper-Raman effect. Analogous to (3.3), we can expand β in a Taylor series in the normal coordinates $q_n = q_{n0} \cos(\omega_n t)$

$$\beta = \beta_0 + \sum_{n=1}^{2Q} \left(\frac{\partial \beta}{\partial q_n} \right)_0 q_n + \dots \quad (3.41)$$

Assume that two laser waves $E_1 = E_{01} \cos(\omega_1 t - k_1 z)$ and $E_2 = E_{02} \cos(\omega_2 t - k_2 z)$ are incident on the Raman sample. From the third term in (3.18a) we then obtain with (3.41) contributions to $p(E)$ due to β_0

$$\beta_0 E_{01}^2 \cos(2\omega_1 t), \quad \text{and} \quad \beta_0 E_{02}^2 \cos(2\omega_2 t), \quad (3.42)$$

which give rise to *hyper-Rayleigh scattering* at frequencies $2\omega_1$, $2\omega_2$ and $\omega_1 + \omega_2$ (Fig. 3.21a). The term $(\partial\beta/\partial q_n)q_{n0} \cos(\omega_n t)$ of (3.41) inserted into (3.18a) yields contributions

$$p^{\text{HR}} \propto \left(\frac{\partial \beta}{\partial q} \right)_0 q_{n0} [\cos(2\omega_1 \pm \omega_n)t + \cos(2\omega_2 \pm \omega_n)t], \quad (3.43)$$

which are responsible for *hyper-Raman scattering* (Fig. 3.21b,c) [3.66].

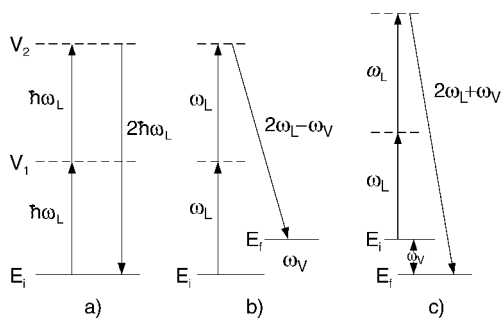


Fig. 3.21a–c. Hyper-Rayleigh scattering (a), Stokes hyper-Raman (b), and anti-Stokes hyper-Raman scattering (c)

Since the coefficients $(\partial\beta/\partial q)_0$ are very small, one needs large incident intensities to observe hyper-Raman scattering. Similar to second-harmonic generation (Vol. 1, Sect. 5.8), hyper-Rayleigh scattering is forbidden for molecules with a center of inversion. The hyper-Raman effect obeys selection rules that differ from those of the linear Raman effect. It is therefore very attractive to molecular spectroscopists since molecular vibrations can be observed in the hyper-Raman spectrum that are forbidden for infrared as well as for linear Raman transitions. For example, spherical molecules such as CH_4 have no pure rotational Raman spectrum but a hyper-Raman spectrum, which was found by Maker [3.67]. A general theory for rotational and rotational–vibrational hyper-Raman scattering has been worked out by Altmann and Strey [3.68].

The intensity of hyper-Raman lines can be considerably enhanced when the molecules under investigation are adsorbed at a surface [3.69], because the surface lowers the symmetry and increases the induced dipole moments.

Similar to the induced Raman effect, the hyper-Raman effect can also be used to generate coherent radiation in spectral ranges where no intense lasers exist. One example is the generation of tunable radiation around $16\text{ }\mu\text{m}$ by the stimulated hyper-Raman effect in strontium vapor [3.70].

3.3.5 Summary of Nonlinear Raman Spectroscopy

In the previous subsections we briefly introduced some nonlinear techniques of Raman spectroscopy. Besides stimulated Raman spectroscopy, Raman gain spectroscopy, inverse Raman spectroscopy, and CARS, several other special techniques such as the Raman-induced Kerr effect [3.71] or coherent Raman ellipsometry [3.72] also offer attractive alternatives to conventional Raman spectroscopy.

All these nonlinear techniques represent coherent third-order processes analogous to saturation spectroscopy, polarization spectroscopy, or two-photon absorption (Chap. 2), because the magnitude of the nonlinear signal is proportional to the third power of the involved field amplitudes (3.18).

The advantages of these nonlinear Raman techniques are the greatly increased signal-to-noise ratio and thus the enhanced sensitivity, the higher spectral and spatial resolution, and in the case of the hyper-Raman spectroscopy, the possibility of measuring higher-order contributions of molecules in the gaseous, liquid, or solid state to the susceptibility.

Additionally, there are several good books and reviews on nonlinear Raman spectroscopy. For more thorough information the reader is therefore referred to [3.11, 3.38, 3.44, 3.48, 3.49, 3.55, 3.57, 3.73].

3.4 Special Techniques

In this section we briefly discuss some special techniques of linear and nonlinear Raman spectroscopy that have particular advantages for different applications. These are the resonance Raman effect, surface-enhanced Raman signals, Raman microscopy, and time-resolved Raman spectroscopy.

3.4.1 Resonance Raman Effect

The Raman scattering cross section can be increased by several orders of magnitude if the excitation wavelength matches an electronic transition of the molecule, that is, when it coincides with or comes close to a line in an electronic absorption band. In this case, the denominator in (3.12) becomes very small for the neighboring lines in this band, and several terms in the sum (3.12) give large contributions to the signal.

The Raman lines appear predominantly at those downward transitions that have the largest Franck–Condon factors, that is, the largest overlap of the vibrational wavefunctions in the upper and lower state (Fig. 3.22). Unlike the nonresonant case, in spontaneous resonance Raman scattering a larger number of Raman lines may appear that are shifted against the excitation line by several vibrational quanta. They correspond to Raman transitions terminating

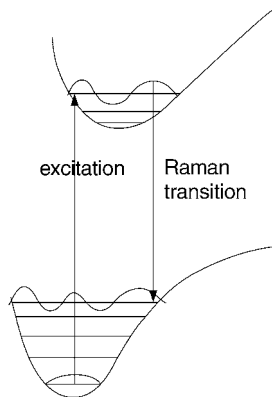


Fig. 3.22. Resonance Raman effect

on higher vibrational levels of the ground electronic state. This is quite similar to laser-excited fluorescence and opens the possibility to determine the anharmonicity constants of the molecular potential curve or potential surface of the lower electronic state.

In stimulated Raman scattering the strongest Raman transition will have the largest gain and reaches threshold before the other transitions can develop. Just above threshold we therefore expect only a single Raman line in the stimulated Raman spectrum, while at higher pump powers more lines will appear.

Resonance Raman scattering is particularly advantageous for samples with small densities, for example, for gases at low pressures, where the absorption of the incident radiation is not severe and where nonresonant Raman spectroscopy might not be sufficiently sensitive.

If the excited state lies above the dissociation limit of the upper electronic state, the scattered Raman light shows a continuous spectrum. The intensity profile of this spectrum yields information on the repulsive part of the potential in the upper state.

3.4.2 Surface-Enhanced Raman Scattering

The intensity of Raman scattered light may be enhanced by several orders of magnitude if the molecules are adsorbed on a surface [3.74]. There are several mechanisms that contribute to this enhancement. Since the amplitude of the scattered radiation is proportional to the induced dipole moment

$$\mathbf{p}_{\text{ind}} = \alpha \cdot \mathbf{E} ,$$

the increase of the polarizability α by the interaction of the molecule with the surface is one of the causes for the enhancement. In the case of metal surfaces, the electric field \mathbf{E} at the surface may also be much larger than that of the incident radiation, which also leads to an increase of the induced dipole moment. Both effects depend on the orientation of the molecule relative to the surface normal, on its distance from the surface, and on the morphology, in particular the roughness of the surface. Small metal clusters on the surface increase the intensity of the molecular Raman lines. The frequency of the exciting light also has a large influence on the enhancement factor. In the case of metal surfaces it becomes maximum if it is close to the plasma frequency of the metal.

Because of these dependencies, surface-enhanced Raman spectroscopy has been successfully applied for surface analysis and also for tracing small concentrations of adsorbed molecules [3.74].

3.4.3 Raman Microscopy

For the nondestructive investigation of very small samples, for example, parts of living cells or inclusions in crystals, the combination of microscopy and Raman spectroscopy turns out to be a very useful technique. The laser beam is focused into the sample and the Raman spectrum that is emitted from the

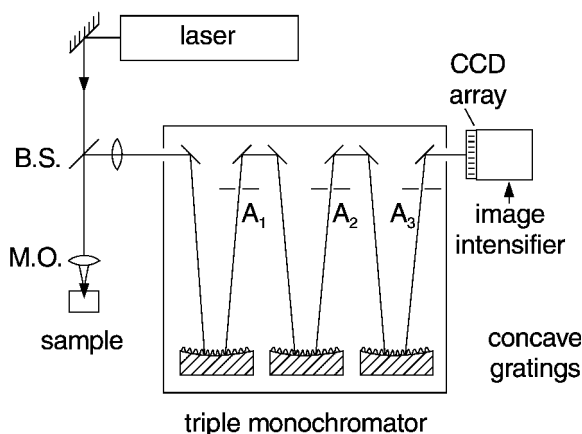


Fig. 3.23. Raman microscopy with suppression of scattered laser light by a triple monochromator with three apertures A_i

small focal spot is monitored through the microscope with subsequent spectrometer. This also applies to measurements of phase transitions in molecular crystals under high pressures. These pressures, which reach up to several gigapascals, can be realized with moderate efforts in a small volume between two diamonds with area A that are pressed together by a force F producing a pressure $p = F/A$. For example, with $F = 10^3$ Pa and $A = 10^{-6}$ cm², one obtains a pressure of 10^9 Pa. The phase transitions lead to a frequency shift of molecular vibrations, which are detected by the corresponding shift of the Raman lines [3.75].

One example of the application of this technique is the investigation of different phases of “fluid inclusions” in a quartz crystal found in the Swiss Alps. Their Raman spectra permitted determination of CO₂ as a gaseous inclusion and water as a liquid inclusion, and they showed that the mineral thought to be CaSO₄ was in fact CaCO₃ [3.76].

A typical experimental arrangement for Raman microscopy is shown in Fig. 3.23. The output beam of an argon laser or a dye laser is focused by a microscope objective into the microsample. The backscattered Raman light is imaged onto the entrance slit of a double or triple monochromator, which effectively suppresses scattered laser light. A CCD camera at the exit of the monochromator records the wanted spectral range of the Raman radiation [3.74, 3.77, 3.78].

3.4.4 Time-Resolved Raman Spectroscopy

Both linear and nonlinear Raman spectroscopy can be combined with time-resolved detection techniques when pumping with short laser pulses [3.79]. Since Raman spectroscopy allows the determination of molecular parameters from measurements of frequencies and populations of vibrational and

rotational energy levels, time-resolved techniques give information on energy transfer between vibrational levels or on structural changes of short-lived intermediate species in chemical reactions. One example is the vibrational excitation of molecules in liquids and the collisional energy transfer from the excited vibrational modes into other levels or into translational energy of the collision partners. These processes proceed on picosecond to femtosecond time scales [3.78, 3.80].

Time-resolved Raman spectroscopy has proved to be a very useful tool to elucidate fast processes in biological molecules, for instance, to follow the fast structural changes during the visual process where, after photoexcitation of rhodopsin molecules, a sequence of energy transfer processes involving isomerization and proton transfer takes place. This subject is treated in more detail in Chap. 6 in comparison with other time-resolved techniques.

3.5 Applications of Laser Raman Spectroscopy

The primary object of Raman spectroscopy is the determination of molecular energy levels and transition probabilities connected with molecular transitions that are not accessible to infrared spectroscopy. Linear laser Raman spectroscopy, CARS, and hyper-Raman scattering have very successfully collected many spectroscopic data that could not have been obtained with other techniques. Besides these basic applications to molecular spectroscopy there are, however, a number of scientific and technical applications of Raman spectroscopy to other fields, which have become feasible with the new methods discussed in the previous sections. We can give only a few examples.

Since the intensity of spontaneous Raman lines is proportional to the density $N(v_i, J_i)$ of molecules in the initial state (v_i, J_i) , Raman spectroscopy can provide information on the population distribution $N(v_i, J_i)$, its local variation, and on concentrations of molecular constituents in samples. This allows one, for instance, to probe the temperature in flames or hot gases from the rotational Raman spectra [3.81–3.84] and to detect deviations from thermal equilibrium.

With CARS the spatial resolution is greatly increased, in particular if BOX CARS is used. The focal volume from which the signal radiation is generated can be made smaller than 0.1 mm^3 [3.54]. The local density profiles of reaction products formed in flames or discharges can therefore be accurately probed without disturbing the sample conditions. The intensity of the stimulated anti-Stokes radiation is proportional to N^2 (3.31). Figure 3.24 shows for illustration the H_2 distribution in a horizontal Bunsen flame, measured from the CARS spectrum of the Q branch in H_2 . The H_2 molecules are formed by the pyrolysis of hydrocarbon molecules [3.58]. Another example is the measurement of CARS spectra of water vapor in flames, which allowed one to probe the temperature in the postflame region of a premixed CH_4 air flame [3.82].

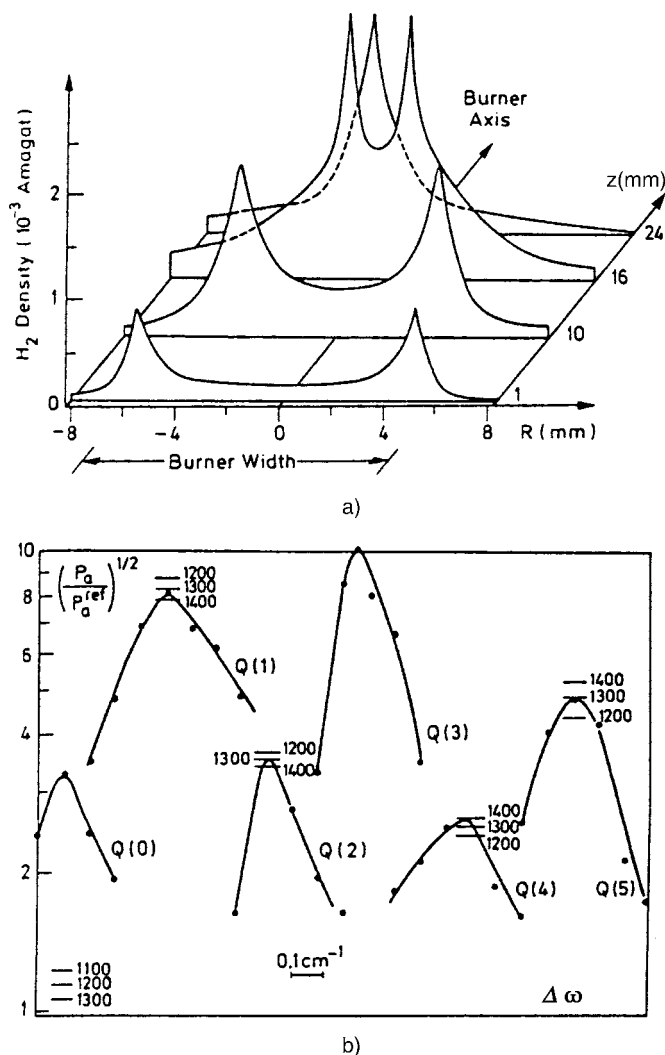


Fig. 3.24a,b. Determination of density profiles of H_2 molecules in a flame. R is the distance from the burner axis, z the distance along this axis. The profiles in (a) have been obtained from the spatial variations of the Q line intensities and spectral profiles shown in (b). The relative intensities of $Q(J)$ furthermore allow the determinations of the temperature profiles. The numbers with the horizontal lines give the expected signal heights for the labeled temperatures T in [K] [3.58]

With a detection sensitivity of 10 to 100 ppm, CARS is not as good as some other techniques in monitoring pollutant gases at low concentrations (Sect. 1.2), but its advantage is the capability to examine a large number of species quickly by tuning the dye lasers. The good background rejection allows the use of this technique under conditions of bright background ra-

diation where other methods may fail [3.83]. Examples are temperature and concentration measurements of molecular nitrogen, oxygen, and methane in a high-temperature furnace up to 2000 K [3.84], where the thermal radiation is much stronger than laser-induced fluorescence. Therefore CARS is the best choice because the detector can be placed far from the furnace.

A further example of the scientific application of CARS is the investigation of cluster formation in supersonic beams (Sect. 4.3), where the decrease in the rotational and vibrational temperatures during the adiabatic expansion (Sect. 4.2) and the degree of cluster formation in dependence on the distance from the nozzle can be determined [3.85].

CARS has been successfully used for the spectroscopy of chemical reactions (Sect. 8.4). The BOX CARS technique with pulsed lasers offers spectral, spatial, and time-resolved investigations of collision processes and reactions, not only in laboratory experiments but also in the tougher surroundings of factories, in the reaction zone of car engines, and in atmospheric research (Sect. 10.2 and [3.86, 3.87]).

The detection sensitivity of CARS ranges from $0.1\text{--}100\text{ ppm}$ ($\hat{= } 10^{-7} - 10^{-4}$ relative concentrations) depending on the Raman cross sections. Although other spectroscopic techniques such as laser-induced fluorescence or resonant two-photon ionization (Sect. 1.2) may reach higher sensitivities, there are enough examples where CARS is the best or even the only choice, for instance, when the molecules under investigation are not infrared active or have no electronic transitions within the spectral range of available lasers.

Further information on laser Raman spectroscopy can be found in [3.88–3.91].

Problems

3.1 What is the minimum detectable concentration N_i of molecules with a Raman scattering cross section $\sigma = 10^{-30}\text{ cm}^2$, if the incident cw laser has 10 W output power at $\lambda = 500\text{ nm}$ that is focused into a scattering volume of $5\text{ mm} \times 1\text{ mm}^2$, which can be imaged with 10% collection efficiency onto a photomultiplier with the quantum efficiency $\eta = 25\%$? The multiplier dark current is 10 photoelectrons per second and a signal-to-noise ratio of 3:1 should be achieved.

3.2 The bent water molecule H_2O has three normal vibrations. Which of these are Raman active and which are infrared active? Are there also vibrations that are both infrared as well as Raman active?

3.3 A small molecular sample of 10^{21} molecules in a volume of $5\text{ mm} \times 1\text{ mm}^2$ is illuminated by 10 W of argon laser radiation at $\lambda = 488\text{ nm}$. The Raman cross section is $\sigma = 10^{-29}\text{ cm}^2$ and the Stokes radiation is shifted by 1000 cm^{-1} . Calculate the heat energy dW_H/dt generated per second in the sample, if the molecules do not absorb the laser radiation or the the

Stokes radiation. How much is dW_H/dt increased if the laser wavelength is close to resonance of an absorbing transition, causing an absorption coefficient $\alpha = 10^{-1} \text{ cm}^{-1}$?

3.4 Estimate the intensity of Raman radiation emerging out of the endface of an optical fiber of 100-m length and 0.1 – mm \varnothing , filled with a Raman-active medium with a molecular density $N_i = 10^{21} \text{ cm}^{-3}$ and a Raman scattering cross section of $\phi_R = 10^{-30} \text{ cm}^2$, if the laser radiation (1 W) and the Raman light are both kept inside the fiber by total internal reflection.

3.5 The two parallel incident laser beams with a Gaussian intensity profile are focused by a lens with $f = 5 \text{ cm}$ in a BOX CARS arrangement into the sample. Estimate the spatial resolution, defined by the halfwidth $S_A(z)$ of the CARS signal, when the beam diameter of each beam at the lens is 3 mm and their separation is 20 mm.